ELSEVIER

Materials Science and Engineering A 474 (2008) 148–156

MATERIALS SCIENCE & ENGINEERING A

www.elsevier.com/locate/msea

Optimization of the LENS® process for steady molten pool size

L. Wang [a], S. Felicelli [b,*], Y. Gooroochurn [c], P.T. Wang [a], M.F. Horstemeyer [a]

[a] *Center for Advanced Vehicular Systems, Mississippi State University, Mississippi State, MS 39762, United States*
[b] *Mechanical Engineering Department, Mississippi State University, Mississippi State, MS 39762, United States*
[c] *ESI Group, Bloomfield Hills, MI 48304, United States*

Received 18 December 2006; received in revised form 27 March 2007; accepted 27 April 2007

Abstract

A three-dimensional finite element model was developed and applied to analyze the temperature and phase evolution in deposited stainless steel 410 (SS410) during the Laser Engineered Net Shaping (LENS®[1]) rapid fabrication process. The effect of solid phase transformations is taken into account by using temperature and phase dependent material properties and the continuous cooling transformation (CCT) diagram. The laser beam is modeled as a Gaussian distribution of heat flux from a moving heat source with conical shape. The laser power and translational speed during deposition of a single-wall plate are optimized in order to maintain a steady molten pool size. It is found that, after an initial transient due to the cold substrate, the dependency of laser power with layer number is approximately linear for all travel speeds analyzed. The temperature distribution and cooling rate surrounding the molten pool are predicted and compared with experiments. Based upon the predicted thermal cycles and cooling rate, the phase transformations and their effects on the hardness of the part are discussed.

Keywords: Laser Engineered Net Shaping; LENS; Finite element modeling; Thermal analysis

1. Introduction

Laser Engineered Net Shaping (LENS®) [1–6] is a very promising technique for the rapid fabrication of fully dense steel components. This technique was first developed by Sandia National Laboratory and commercialized by Optomec Inc. In the LENS® process, parts are constructed by focusing a laser beam onto the deposition region, where streams of metallic powder are simultaneously injected by the nozzles under computer guidance. The laser locally melts the powder to create a molten pool on the top surface of the growing part. After deposition of each layer, the powder delivery nozzle and the laser beam assembly is raised in the positive *Z*-direction, thereby building a three-dimensional component layer additively.

The microstructural features and mechanical properties of the final part are significantly affected by the cooling rate and solidification velocity at the solid–liquid interface of the molten pool, and by the thermal cycles that may occur during the deposition process. Optimization of the process requires a complete understanding of the complex thermal history during part fabrication. Numerical simulation methods have the potential to provide detailed information of the thermal behavior. Numerical models have been performed by several authors to simulate the temperature history [3–8] and microstructure evolution [9–11] during the LENS® process.

The molten pool size has been identified as a critical parameter for maintaining optimal build conditions [2]. The effects of the laser-processing parameters (laser power and scanning speed) on the molten pool size have been investigated both by experiments [11] and modeling [12]. For constant laser scanning speed, the geometry of the molten pool depends on the heat input distribution. During operation of the LENS® machine, real-time thermal images of molten pool size are used as a feedback mechanism to control the process [5]. The laser power is adjusted to make sure that the molten pool size is in the pre-defined range during the fabrication process.

In the present work, a three-dimensional finite element model was developed to simulate multilayer LENS® deposition of 410 stainless steel (SS410) powder. Development of the model was carried out using the SYSWELD software package [13–15]. The model considers a Gaussian distribution of heat flux from a moving heat source with a conical shape. The metallurgical transformations with respect to the thermal behavior are taken

* Corresponding author. Tel.: +1 662 325 1201; fax: +1 662 325 7223.
E-mail address: felicelli@me.msstate.edu (S. Felicelli).
[1] LENS® is a registered trademark of Sandia Corporation.

0921-5093/$ – see front matter © 2007 Elsevier B.V. All rights reserved.
doi:10.1016/j.msea.2007.04.119

into account using the temperature dependent material properties and the continuous cooling transformation (CCT) diagram. In this study, the temperature distribution and cooling rate surrounding the molten pool were predicted and compared with experimental data available in the literature [3]. The laser power and travel speed were optimized in order to achieve a pre-defined molten pool size for each layer. The thermal cycles and cooling rates at different locations were calculated for a 10-pass LENS® process. Finally, based upon the predicted thermal cycles and cooling rates, the phase transformations and their effect on the material hardness are discussed.

2. Finite element modeling

A three-dimensional finite element model was developed to simulate the LENS® process using the commercial code SYSWELD. The model was used to predict the temperature distribution and cooling rate for the LENS® process of a thin-walled structure (plate) of AISI 410 stainless steel (SS410). The geometry and finite element mesh used in the model are shown in Fig. 1.

The structure was built by overlapping 10 single tracks of material, each with a length of 10.0 mm, a thickness of 0.5 mm and a width of 1.0 mm. The plate was fabricated on the surface of a substrate having 5 mm thick, 10 mm wide and 20 mm long. The travel speed of the laser beam is 7.62 mm/s. The laser beam moves in the same direction (left to right) for each pass. A dense mesh was used for the plate and the contact area with the substrate, where higher thermal gradients are expected. An optimized time-stepping scheme was employed to achieve fast convergence of the solution and reasonable accuracy.

It was assumed that the initial temperature of the substrate was 20 °C (no preheating). The time needed for each pass is 2 s. The idle time between the depositions of consecutive layers is 0.7 s. SS410 is used for both the substrate and the deposited plate. The chemical composition of SS410 is summarized in Table 1.

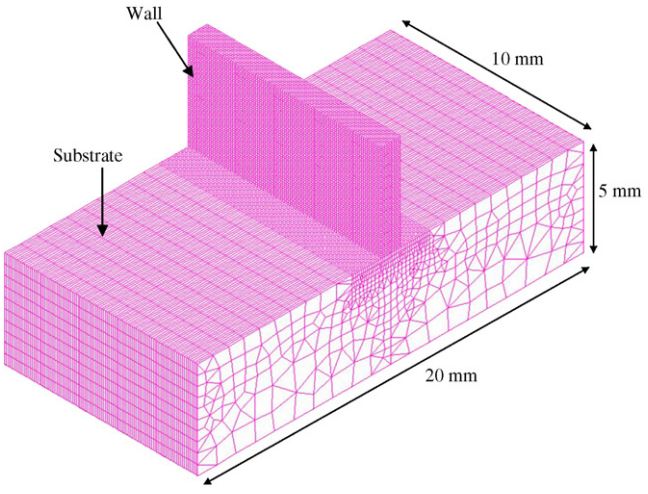

Fig. 1. Finite element mesh and geometry to simulate the LENS® process for a 10-layer plate.

Table 1
Chemical composition of SS410 steel (wt.%)

C	Si	Mn	Cr	P	S
0.12/0.17	<1.0	<1.0	12.0/14.0	<0.04	<0.03

2.1. Heat transfer equation

To calculate the temperature distribution, the finite element method was used to numerically solve the following heat conduction equation:

$$\left(\sum_i P_i(\rho C_p)_i\right)\frac{\partial T}{\partial t}-\nabla\left(\left(\sum_i P_i\lambda_i\right)\nabla T\right)+\sum_{i<j}L_{ij}A_{ij}=0 \quad (1)$$

where T is temperature, t is time, P_i is the volume fraction of phase i, ρ is density, C_p is specific heat, λ is thermal conductivity, L_{ij} is the latent heat of the transformation from phase i to j, and A_{ij} is the fraction of phase i transformed to j per unit time. The calculation of temperature evolution is fully coupled with the prediction of phase transformation. Three micro structures, ferrite, martensite, and austenite, are used in the analysis. The austenitic grain size effect was neglected. The density, thermal conductivity, and specific heat are dependent on temperature and material phase, as shown in Fig. 2. The latent heat effects due to phase changes are modeled with the specific heat variation, as shown in Fig. 2(c).

2.2. Heat input

In order to simulate the heat input distribution, the laser beam is modeled as a Gaussian profile of heat flux produced by a moving heat source with a conical shape. During the LENS® process, part of the energy generated by the laser beam is lost before being absorbed by the deposited material. Measurements in Ref. [16] revealed that the laser energy transfer efficiency was in the range of 30–50%. This indicates that more than half of the incident laser energy is never transferred to the deposited material. Several factors can reduce the net absorbed laser energy: partial reflection on the deposited metal, absorption by in-flight powder, absorption by evaporating metal from the pool, and dependence of the absorptivity of the material on temperature and laser wavelength. Furthermore, other complex phenomena occur in the molten pool, such as phase transition (e.g., melting and evaporation) and Marangoni convection, which are not taken into account in the current study.

In this work, the nominal laser power is calibrated by matching the thermal profile surrounding the molten pool with the experimental data of Ref. [3]. The Gaussian distribution of heat flux can be computed according to the formula [17]:

$$Q_r = \frac{2P}{\pi r_0^2 H}\left(1-\frac{z}{H}\right)\exp\left(1-\left(\frac{r}{r_0}\right)^2\right) \quad (2)$$

where Q_r is the input energy density (W/mm^3), P the absorbed laser beam power (W), and r_0, H, r, and z are parameters that

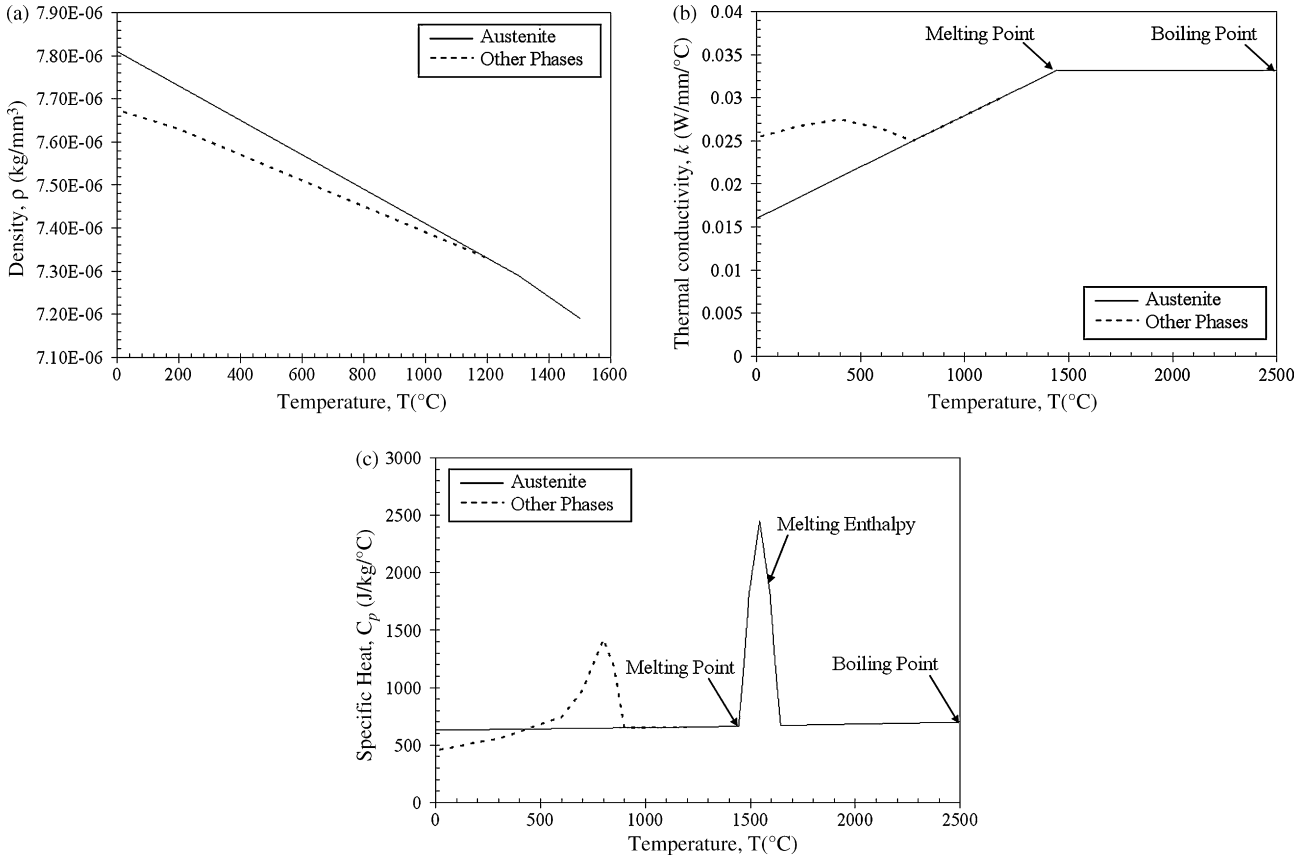

Fig. 2. Thermal properties used for SS410, (a) density, (b) thermal conductivity, (c) specific heat.

characterize the shape of the laser beam. The moving heat source was modeled by a user subroutine in SYSWELD code.

2.3. The dummy material method

The model uses a fixed mesh for the plate and substrate, where the elements of the plate are initially inactive and are activated during material deposition. Two different approaches are available to model material deposit in SYSWELD. One is activation/deactivation of element, which uses a formulation to activate and deactivate the elements; another is dummy material method. In the current study, dummy material method that uses three different types of material is employed for the element activation. The first material is used for the substrate and the elements of layers that have already been deposited; this material is assigned the actual thermal and metallurgical properties of SS410. The initial phase for the substrate is assumed to be ferrite. Austenitization may occur when the temperature exceeds the austenitization temperature. The martensitic and ferritic transformations may occur during cooling in the substrate and in the layers that have been deposited, depending on the cooling rate and temperatures. The second material is used for elements of layers that have not yet been deposited. These elements are assigned dummy low values of the thermal properties, which means that the material cannot be heated up, therefore cannot transform to austenite. No metallurgical properties (phase transformations) are required for the second material. A third type of material is used for the elements that are being deposited. These elements are initially in the dummy phase but they are assigned the actual thermal properties of SS410 so that they can heat up. Once they reach the austenization temperature, the dummy phase is switched to austenite and the actual metallurgical behavior (subsequent transformation to martensite or ferrite) is modeled after that. A graphical representation of the different material types is shown in Fig. 3.

2.4. Initial and boundary conditions

The initial condition in the computational domain is set to a uniform temperature field.

$$T(x, y, z, t = 0) = T_0 \tag{3}$$

An essential boundary condition is imposed on the bottom surface of the substrate, given by:

$$T(x, y, z = 0) = T_0 \quad \text{for } t > 0 \tag{4}$$

The boundary conditions for all other surfaces take into account both the laser heating and heat losses due to convection and radiation

$$k(\nabla T \cdot \vec{n})|_{\Omega} = h(T - T_{\mathrm{a}})|_{\Omega} + \varepsilon\sigma(T^4 - T_{\mathrm{e}}^4)|_{\Omega} - Q_{\mathrm{r}}|_{\Omega\,\mathrm{Laser}} \tag{5}$$

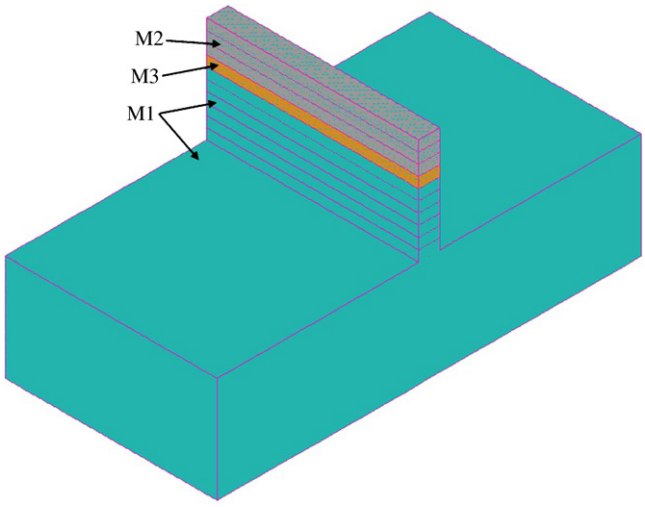

Fig. 3. Sketch to illustrate dummy material method for the element activation. M1: deposited layers and substrate; M2: layers to be deposited; M3: layer being deposited.

where k is the thermal conductivity, h the convective heat transfer coefficient, T_a is the ambient temperature around the part, which is considered to be equal to room temperature, ε the emissivity of the part surface, σ the Stefan–Boltzmann constant [$\sigma = 5.67 \times 10^{-8}$ W/m^2 K^4], T_e the temperature of the internal wall of the glove box (taken equal to T_a in this work), and Q_r is the heat input from the laser beam, as shown in Eq. (2). As new elements are activated, the surfaces exposed to boundary conditions are updated.

3. Results and discussions

In lack of available experimental data with SS410, we used the experiments of Hofmeister et al. [3] for correlation purposes. In these experiments, ultra-high speed digital imaging techniques were employed to analyze the image of the molten pool and the temperature gradient on the surface surrounding the molten pool in SS316 samples fabricated using LENS®. SS316 and SS410 have similar thermal properties and in our calculations, we use computational process parameters that approximate the conditions of Hofmeister's experiments. The calculation is performed only for the deposition of the top layer

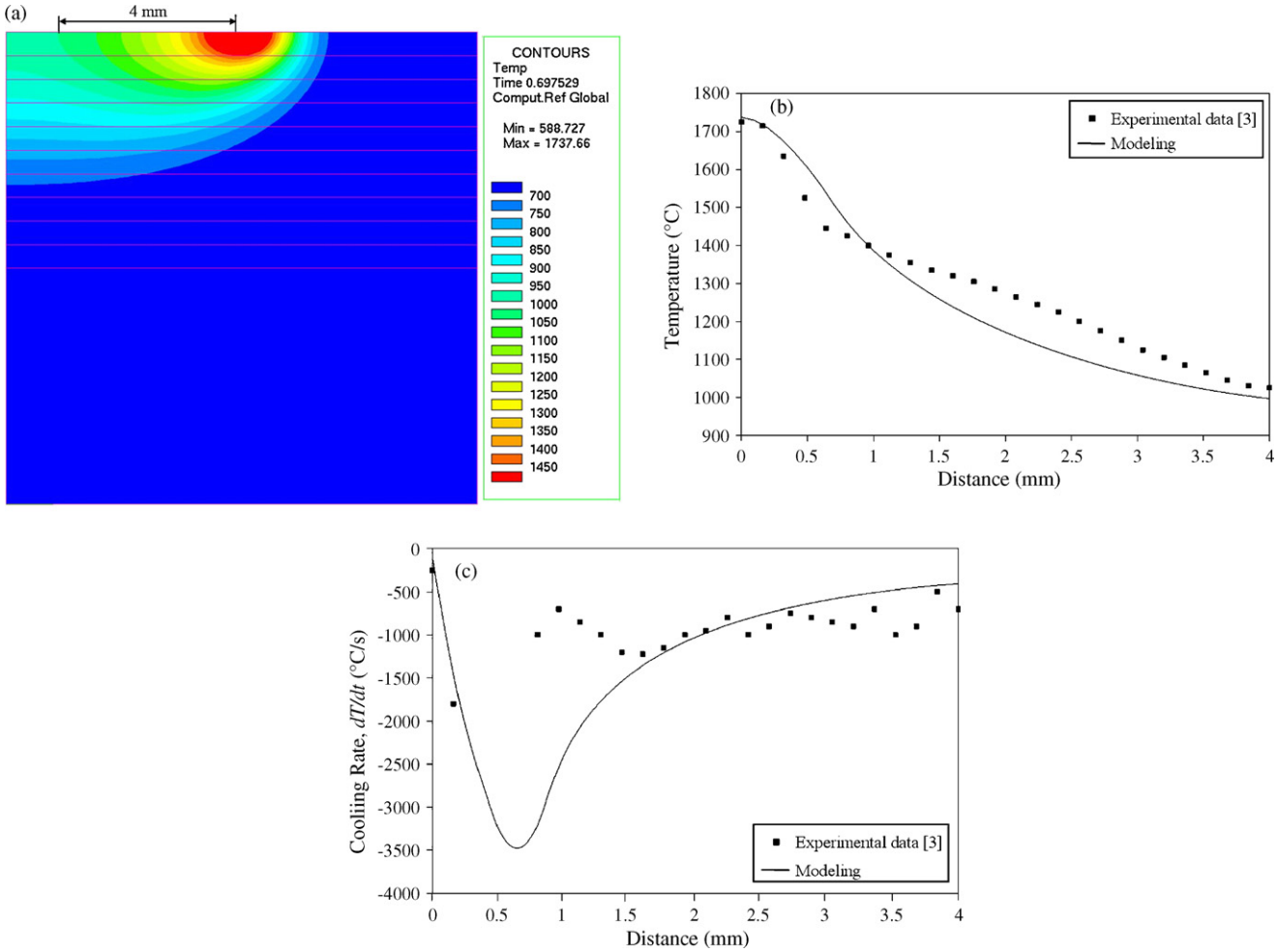

Fig. 4. (a) Calculated temperature distribution during deposition of SS410. (b and c) Model and experiment comparison of temperature profile (b) and cooling rate (c). The profiles are shown from the center of the molten pool along the travel direction of deposited part.

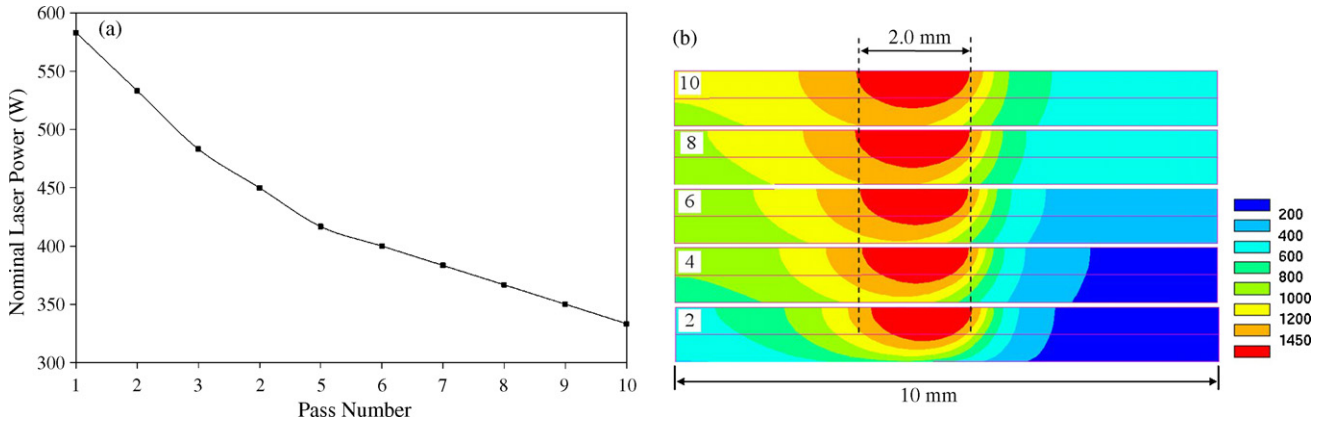

Fig. 5. (a) Nominal laser powers for each pass to achieve a steady molten pool size; (b) molten pool size and shape when the laser beam moves to the center of the part for layers 2, 4, 6, 8, and 10. The average size of the molten pool is 2.0 mm. The molten pool size is determined by the melting temperature of SS410 (1450 °C).

(the 10th layer), using the experimental temperature data as initial condition for the previously built layers.

Fig. 4(a) shows the temperature distribution when the laser beam moves to the center of the top layer and side effects can be neglected. The comparisons of measured and predicted temperature profile (Fig. 4(b)) and cooling rate (Fig. 4(c)) have been performed on the top surface of the part, from the center of the molten pool along the travel direction of the fabricated part, which is opposite to the moving direction of the laser beam. The inputs used to generate the results were an absorbed laser power of $P = 100$ W and an initial temperature of 600 °C for the substrate and deposited part before the 10th layer is deposited. The travel speed of the laser beam is 7.62 mm/s. Measurements were made for the nominal laser power of 275 W by Hofmeister et al. [3]. Therefore, the laser energy transfer efficiency is 36.4%, which is consistent with experimental data reporting a range of 30–50% [16]. It is observed from Fig. 4(b) and (c) that the calculated temperature profile follows rather well the experimental data, with an error less than 8%. The calculated and measured cooling rate also compare well in the region away from the molten pool, but the model predicts a higher cooling rate as we get closer to the pool, with the highest predicted value being in the liquid next to the solid–liquid interface. Unfortunately the experimental data in this region is scarce and does not exhibit a well-defined trend as to allow a more detailed comparison with calculations.

The calibrated model was then used to simulate the complete 10-pass LENS® process. The laser power is adjusted for each pass in order to achieve a steady molten pool size and temperature distribution surrounding the molten pool. Fig. 5(a) shows the nominal laser powers applied for each pass. The nominal laser power is obtained by considering that the laser energy transfer efficiency is 36.4%, as mentioned above. It is observed that the nominal laser power required to keep a fairly constant pool size decreases as more layers are deposited. During deposition of the first few layers, higher power is needed to compensate for the heat dissipation by the cold substrate. As more layers are deposited, they act as a barrier to heat conduction to the substrate, the part becomes hotter and less power is needed for subsequent deposition. It is also observed in Fig. 5(a) that after deposition of the first five layers, the laser power necessary to maintain the pool size decreases approximately linearly for the subsequent layers. This indicates that the initial transient produced by the cold substrate affects only the first five layers.

Fig. 5(b) shows the molten pool size when the laser beam moves to the center of the plate for each layer. It can be seen that the molten pool size is approximately the same for each pass. About one and a half layers are melted for each pass. The steady

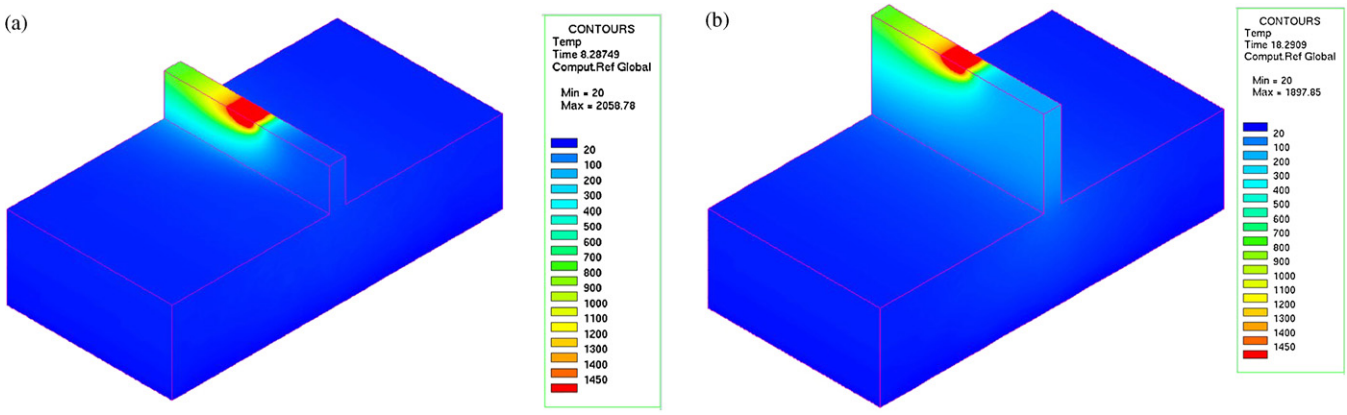

Fig. 6. Three-dimensional temperature distributions when the laser beam moves to the center of (a) the part 5th layer, and (b) the 10th layer of the deposited plate.

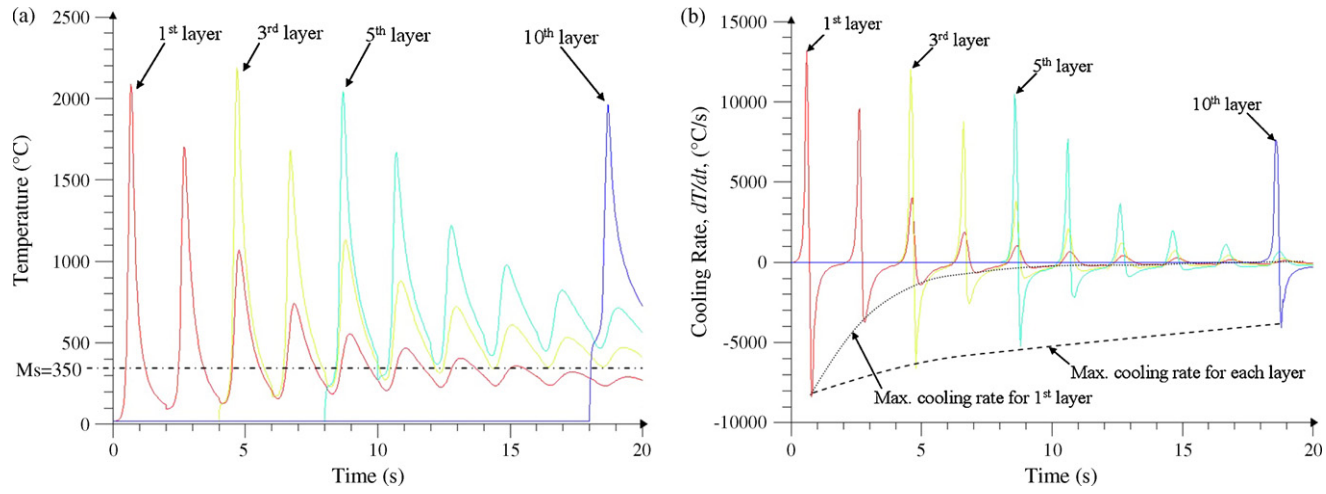

Fig. 7. (a) Thermal cycles, and (b) cooling rates for the midpoints of layers 1, 3, 5, and 10 of the built profile as a function of time.

molten pool geometry indicates relatively steady temperature distribution for each pass, which results in rather uniform phase proportions and microstructure for the finished part.

The three-dimensional temperature distributions are shown in Fig. 6 when the laser beam moves to the center of the fifth layer (Fig. 6(a)) and the tenth layer (Fig. 6(b)) of the plate. Similar molten pool size and temperature distribution surrounding the molten pool are obtained for both cases. The previous layers are reheated when the subsequent layer is deposited.

Fig. 7(a) shows the thermal cycles at the mid-points of deposited layers 1, 3, 5, and 10. Each peak indicates that the laser beam passes over or near the pre-defined location, from initial layer to subsequent layer depositions. At the mid-point of the first layer, the initial peak in temperature is approximately 2100 °C. After that, the heat is quickly conducted away to around 100 °C at $t = 2$ s for the first layer. This indicates that the idle time between the depositions of the first two consecutive layers is enough to cool down the deposited part. The solidification process in the initial thermal cycle during the first pass should result in a high strength, martensitic microstructure with minimal retained ferrite due to the high cooling rate. However, each subsequent pass reheats the previous layers to above the martensite starting temperature (Ms = 350 °C for SS410 [18]), which results in the tempered martensite transformation. After the fifth layer is deposited, the first layer still receives a thermal hit of 550 °C. After each deposition pass, the part cools down, but the part receives an integrated heat, which can affect the material properties including residual stress and mechanical strength due to tempering or aging effects [6].

The mid-points of the layers 3, 5, and 10 have experienced similar thermal cycles as the midpoint of the first layer. The maximum temperatures of the mid-points in each layer are approximately the same. For the first five layers, the thermal cycles due to the reheat of subsequent passes will result in the transformation of tempered martensite. After the fifth layer is deposited, however, the temperatures at the upper part can never cool down to the martensite starting temperature. Therefore, for the upper part, martensite cannot be transformed during the deposition process, and fresh martensite will be transformed when the part is finished, which is consistent with the investigation of other researchers [5,9]. The possible tempered martensitic transformation of the lower layers will cause the hardness of the upper part to be higher than that of the lower part.

Fig. 7(b) shows the cooling rates at the mid-points of the layers 1, 3, 5, and 10. The positive peaks indicate that the pre-defined location is heated up when the laser beam passes over, and the negative peaks indicate that the pre-defined location cools down after the laser beam passes by, from the initial layer to subsequent layer depositions. At the mid-point of the first layer, the initial maximum cooling rate is approximately 8000 °C/s. After that, the maximum cooling rate in the first layer decreases when the subsequent layers are deposited. After the third layer is deposited, the first layer still receives a maximum cooling rate of 1000 °C/s. The midpoints of the layers 3, 5, and 10 have experienced similar cooling curves as the mid-point of the first layer. The maximum cooling rate for each pass decreases as more layers are deposited, which is due to the integrated heat of the substrate and previous layers.

In Figs. 8–11, we study the effect of translational laser speed on the temperature profile and cooling rate. We compare results for three values of travel speed: 2.5, 7.62, and 20 mm/s. In all

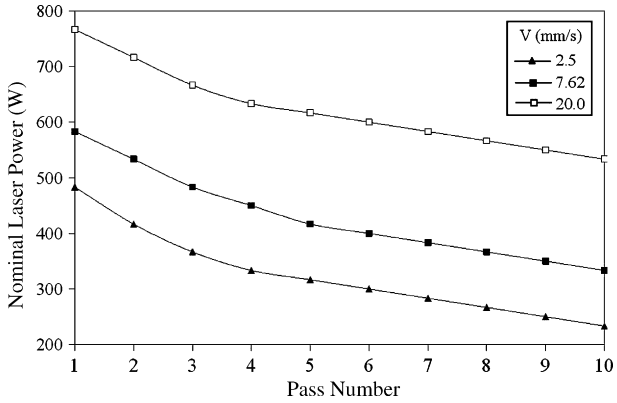

Fig. 8. Nominal laser power distribution for each pass for different laser travel velocities.

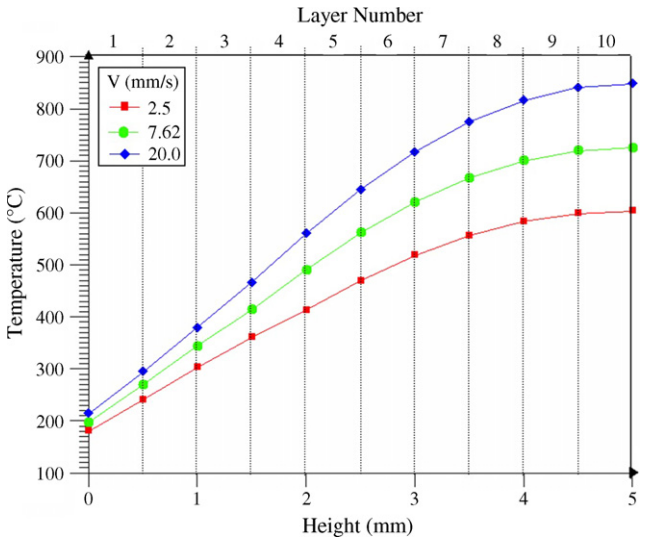

Fig. 9. Temperature along the plate height center line, for different laser travel velocities. The plotted data refers to the time instant after the 10th layer is deposited.

these calculations, it is assumed that the powder flow rate is correspondingly adjusted so that the same layer thickness of 0.5 mm is maintained during the deposition. The model is then used to calculate the necessary laser power to maintain a steady size of the molten pool. Fig. 8 shows the required power profiles as a function of the layer number and laser speed. It is observed that the same trend described in Fig. 5(a) is maintained for the other two values of travel speed, i.e., the dependency of laser power versus layer number is approximately linear after deposition of the 5th layer. In addition, the decrease rate is similar (about 16.7 W/layer) for the three values of travel speed. However, the laser power must increase with translational velocity in order to maintain the same pool size.

Fig. 9 shows the vertical temperature profile along the midline of the plate as a function of laser speed. The temperature values correspond to the time instant after the 10th layer has been deposited. The three profiles look similar, with higher temperature for faster speed because of the corresponding higher power. Observe the rapid decrease of the vertical temperature gradient near the top surface, which causes a difference of more than 200 °C at this location between the lowest and highest speeds. However, the temperature at the base of the plate is similar for the three speeds.

The thermal cycling at the midline of the plate produced by successive layer depositions is shown in Fig. 10. The layer color convention is the same as used in Fig. 7 and the labels are not repeated for clarity. It is observed that similar profiles of temperature and cooling rate are obtained for the three speeds, but with a different time scale. Note that higher translational speed results in significantly higher cooling rate but in slightly lower peak temperatures. Also note that for the highest speed, the maximum cooling rate (negative peaks in Fig. 10(c)) stays basically constant after the third layer, in contrast with the decreasing tendency observed for lower speeds. The results of Fig. 10 would seem to favor the deposition at high speeds because of high cooling rates, finer microstructure and higher production yield. Unfortunately, there are operational difficulties not considered in this study which limit the processing at too high speeds; for example, the entrapment of pores because of incomplete powder melting.

In Fig. 11, a vertical cross section of the plate is shown, with temperature contours for the different travel velocities. As done in Fig. 5, the size of the molten pool is indicated by the 1450 °C

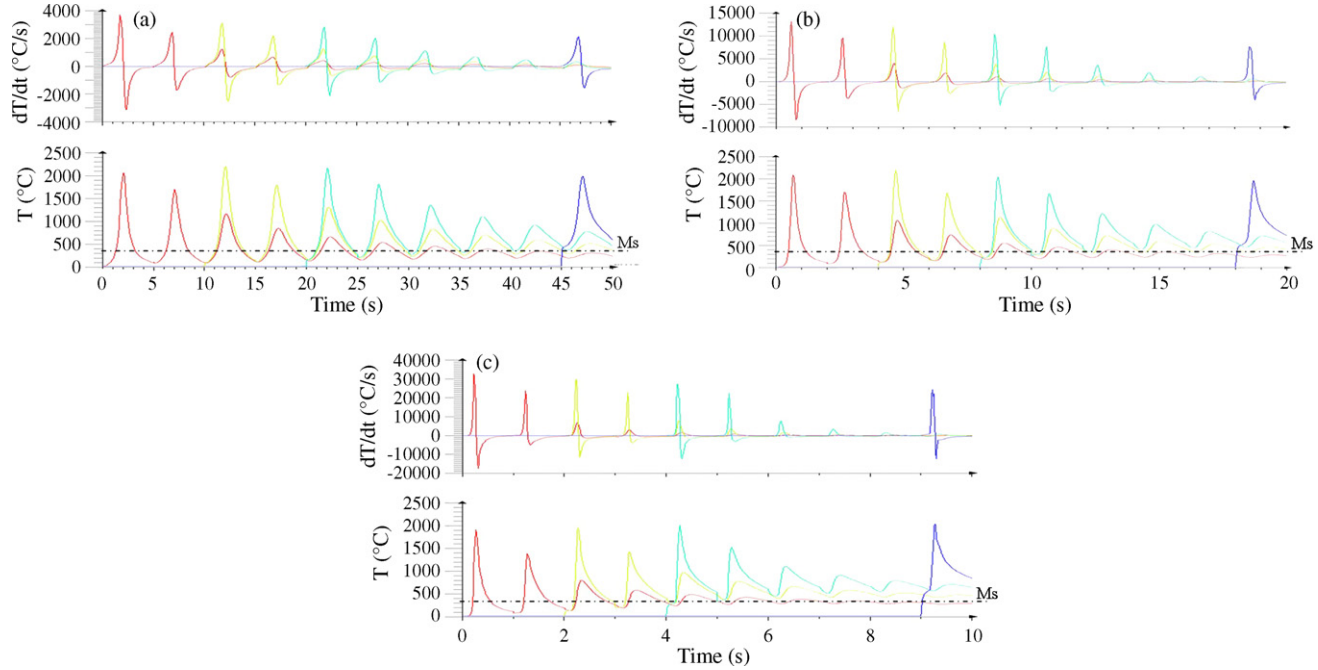

Fig. 10. Thermal cycles and cooling rates for the midpoints of layers 1, 3, 5, and 10 of the built profile varies with time. (a) $V = 2.5$ mm/s; (b) $V = 7.62$ mm/s; (c) $V = 20.0$ mm/s.

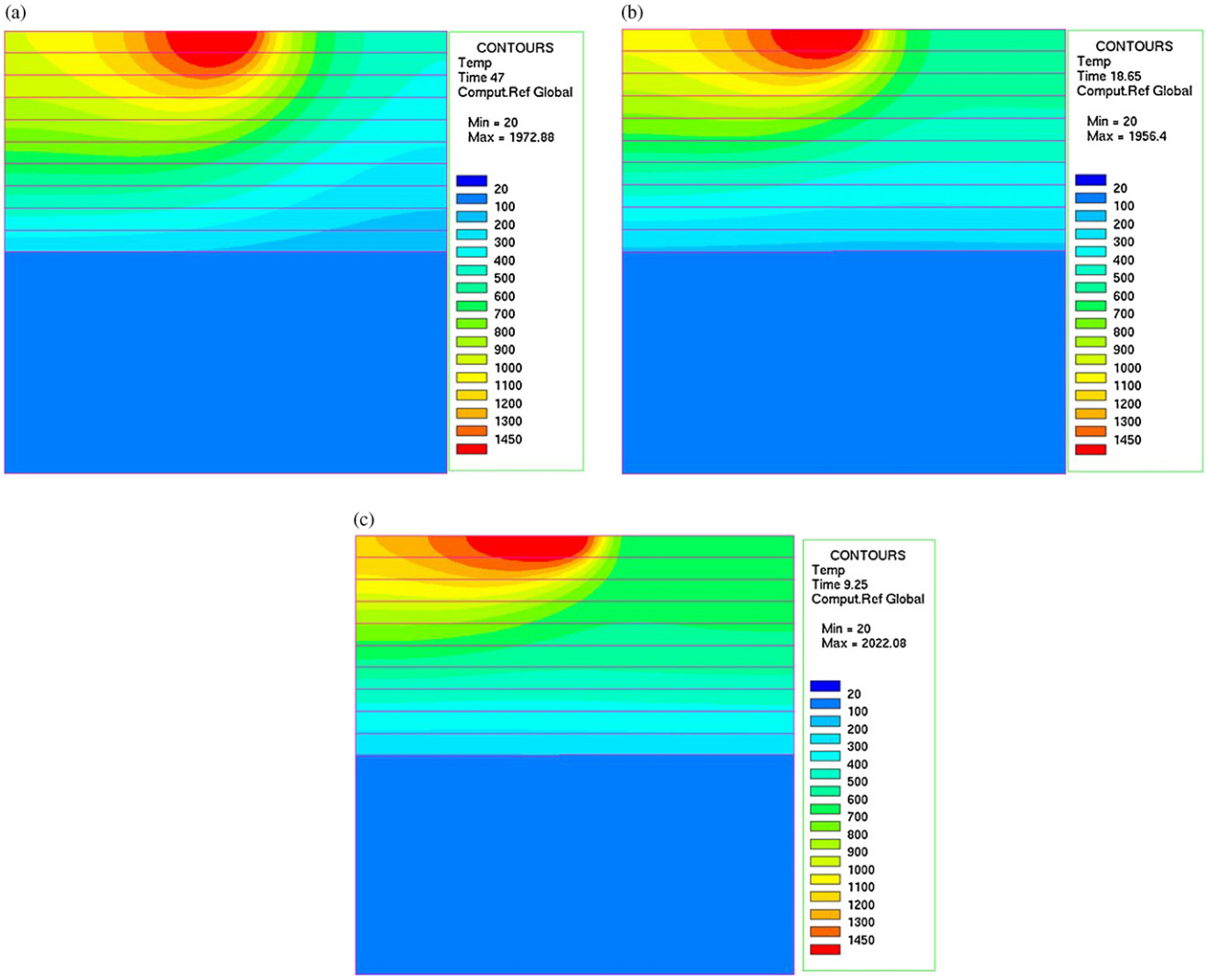

Fig. 11. Temperature distributions when the laser beam moves to the center of the top surface at the 10th layer for different velocities. (a) $V = 2.5$ mm/s; (b) $V = 7.62$ mm/s; (c) $V = 20.0$ mm/s.

contour (melting temperature of SS410). It is observed that for the highest speed (Fig. 11(c)), the shape of the pool has become elongated and it hardly penetrates into the second layer. More power is still needed to maintain a similar penetration to that in the lower speed cases of Fig. 11(a) and (b).

4. Conclusions

A three-dimensional finite element model has been developed to simulate the LENS® process of SS410. The finite element calculations were performed using the SYSWELD software tool, which takes into account temperature dependent material properties and phase transformations. It considers a moving heat source of Gaussian profile in a conical shape. The model was first correlated with published experimental data and good agreement was achieved with calculated results. Then the model was used to analyze the heat transfer during the 10-pass fabrication of a SS410 plate. The objective of the analysis was to find the power program required to maintain a predetermined molten pool size during the entire deposition process. A second objective was to determine how the power program is affected by the laser travel speed. It was found that, after an initial transient due to the cold substrate, the dependency of required laser power with layer number is approximately linear, with similar decrease rates for all travel speeds analyzed. However, the laser power must increase with translational velocity in order to maintain the same pool size. The application of these power programs will keep the molten pool size in the predefined range, which results in steady temperature distribution surrounding the molten pool and a relatively uniform microstructure of the final part. Several aspects of the thermal phenomena that occur during the LENS® process were discussed in the article, including solid phase transformations and their effect on the distribution of hardness in the fabricated part.

Acknowledgments

The authors appreciate the sponsorship of the U.S. Army TACOM and the Center for Advanced Vehicular Systems

(CAVS). We would like to thank Dr. John Berry of Mississippi State University, Jim Bullen of Optomec Inc. and Benton Gady of National Automotive Center (NAC) for their helpful suggestions and guidance in this work.

References

[1] C.L. Atwood, M.L. Griffith, M.E. Schlienger, L.D. Harwell, M.T. Ensz, D.M. Keicher, M.E. Schlienger, J.A. Romero, J.E. Smugeresky, Proceedings of ICALEO '98 November 16–19, Orlando, FL, 1998, p. E-1.
[2] G.K. Lewis, E. Schlienger, Mater. Des. 21 (2000) 417–423.
[3] W. Hofmeister, M. Wert, J. Smugeresky, J.A. Philliber, M. Griffith, M.T. Ensz, JOM 51 (7) (1999).
[4] M.L. Griffith, M.T. Ensz, J.D. Puskar, C.V. Robino, J.A. Brooks, J.A. Philliber, J.E. Smugeresky, W.H. Hofmeister, Mater. Res. Soc. 625 (2000) 9–20.
[5] M.L. Griffith, M.E. Schlienger, L.D. Harwell, M.S. Oliver, M.D. Baldwin, M.T. Ensz, J.E. Smugeresky, M. Essien, J. Brooks, C.V. Robino, W.H. Hofmeister, M.J. Wert, D.V. Nelson, J. Mater. Des. 20 (1999) 107–114.
[6] M.L. Griffith, M.E. Schlienger, L.D. Harwell, M.S. Oliver, M.D. Baldwin, M.T. Ensz, J.E. Smugeresky, M. Essien, J. Brooks, C.V. Robino, W.H. Hofmeister, M.J. Wert, D.V. Nelson, Proceedings of the Solid Freeform Fabrication Symposium, Austin, TX, 1998, pp. 89–97.
[7] R. Ye, J.E. Smugeresky, B. Zheng, Y. Zhou, E.J. Lavernia, Mater. Sci. Eng. A 428 (2006) 47–53.
[8] L. Wang, S.D. Felicelli, Mater. Sci. Eng. A 435–436 (2006) 625–631.
[9] L. Costa, R. Vilar, T. Reti, A.M. Deus, Acta Mater. 53 (2005) 3987–3999.
[10] S.M. Kelly, S.L. Kampe, Metall. Mater. Trans. A 35 (2004) 1869–1879.
[11] M. Labudovic, D. Hu, R. Kovacevic, J. Mater. Sci. 38 (2003) 35–49.
[12] A. Vasinonta, J.L. Beuth, M.L. Griffith, Proceedings of the Solid Freeform Fabrication Symposium August, Austin, TX, 2000.
[13] SYSWELD 2005 Reference Manual, ESI Group, 2005.
[14] SYSWELD 2005 Example Manual, ESI Group, 2005.
[15] SYSTUS 2005 Analysis Reference Manual, ESI Group, 2005.
[16] R.R. Unocic, J.N. DuPont, Metall. Mater. Trans. B 35 (2004) 143–152.
[17] S.A. Tsirkas, P. Papanikos, Th. Kermanidis, J. Mater. Process. Technol. 134 (2003) 59–69.
[18] ASM Handbook, Welding, Brazing, and Soldering, vol. 6, ASM International, Material Park, OH, 2005, p. 438.